Biogeotechnics 4 (2026) 100184

Contents lists available at ScienceDirect

Biogeotechnics

journal homepage: www.keaipublishing.com/en/journals/biogeotechnics/

# Distribution and temporal-spatial characteristics of geohazards in a rainstorm-prone area of SE China considering the land use

Zizheng Guo[a], Yuhua Zhang[b], Luqi Wang[c,d,*], Zhanxu Guo[a], Lu Shi[a], Xinyong Zhou[a], Haojie Wang[a], Mengchen Cheng[a], Guangqi Chen[a]

[a] School of Civil and Transportation Engineering, Hebei University of Technology, Tianjin 300401, China
[b] The Bartlett Centre for Advanced Spatial Analysis, Faculty of the Built Environment, University College London (UCL), London W1T4TJ, UK
[c] School of Civil Engineering, Chongqing University, Chongqing 400045, China
[d] Chongqing Field Scientific Observation Station for Landslide Hazards in Three Gorges Reservoir Area, Chongqing University, Chongqing 400045, China

ARTICLE INFO

*Keywords:*
Geohazard
Tempo-spatial characteristics
GIS
Rainfall
China

ABSTRACT

Geohazards are one of the most important natural hazards worldwide, and they cause massive deaths and large economic losses on a yearly basis. However, the quantification of fatalities and casualties by the geohazards is commonly highly underestimated due to the incomplete or absent database at a national or regional scale. Hence, the analysis regarding the distribution and temporal-spatial characteristics of geohazards over a large area is an urgent task instead of small-scale studies of hotspots. In order to update the new insights within this topic, the present study took Wenzhou City in southeastern China as the test area, which is well known as a rainstorm-prone region subjected to the monsoon from the Pacific. A database incorporating historical geohazards during the past two decades was constructed based on multiple data sources. The relationship between different types of geohazards versus rainfall, administrative areas (second-level administrative scale), and environmental factors was analyzed to reveal the overall distribution characteristics of the geohazards. The results show that there are a total of 1725 geohazards in the area, and the landslides occupies the largest proportion, whereas the numbers of collapses and debris flows are similar. The causes of the most geohazards in the study area can be divided into three types: (i) rainstorm-induced geohazards (max daily rainfall higher than 50 mm), (ii) long-term but low-intensity rainfall (so-called plum rain)-induced geohazards (longer than 3 days and the max daily rainfall lower than 50 mm), and (iii) engineering activities-induced geohazards, such as slope cutting and infrastructure construction projects. Among them, the types (i) and (ii) are commonly characterized as instant failure and rapid run-out, thus posing higher risks for local residents. Additionally, the evident spatial distribution difference of geohazards related to various environmental factors (elevation, slope, soil, and land use) was also observed. These outcomes not only contribute to the risk reduction and mitigation of geohazards in SE China but also provide an essential reference for the prevention of geohazards in other areas with similar settings.

## 1. Introduction

Fatal geohazards have caused thousands of deaths or injuries in East Asia every year, and considerable economic damages to infrastructures and environments (Petley, 2012; Abancó et al., 2021; Shugar et al., 2021). As reported, the East Asia geohazard record is dominated by events in China, especially those triggered by seasonal rainfall and tropical cyclones (Dou et al., 2023; Froude & Petley, 2018; Guo et al., 2020a; Yang et al., 2024). Rainfall infiltration causes a decrease in matric suction, then reduces the shear strength of soil (soil softening), thus resulting in unsaturated soil slope failure (Ni et al., 2018; Ng et al., 2022; Kamran et al., 2023; Guo et al., 2024a; Ng et al., 2024). These events were mostly observed in the southeastern part of China, because it frequently suffered from the monsoon of the Pacific along with heavy rainstorms (Li & Huang, 2023; Ouyang et al., 2018; Qin et al., 2022). However, very few studies have been conducted for quantitative assessment of the tempo-spatial distribution and the impacts of these geohazards, which has limited the knowledge of their mechanisms and risk management.

* Corresponding author.
*E-mail address:* wlq93@cqu.edu.cn (L. Wang).

https://doi.org/10.1016/j.bgtech.2025.100184
Received 23 October 2024; Received in revised form 29 May 2025; Accepted 31 May 2025
Available online 1 June 2025
2949-9291/© 2026 The Authors. Publishing services by Elsevier B.V. on behalf of KeAi Communications Co. Ltd. This is an open access article under the CC BY-NC-ND license (http://creativecommons.org/licenses/by-nc-nd/4.0/).

Preparing geohazard maps is considered an initial step for the analysis of temporal-spatial characteristics, and of high importance to assess geohazard susceptibility, vulnerability, and risk, and to study the evolution of landscapes affected by mass-wasting (Guzzetti et al., 2012). Generally, available inventory for geohazards at a global or national scale can be divided into two categories: event-based inventory and historical geohazard inventory (Zhang et al., 2023). The former focuses on the geohazards triggered by specific events (e.g., rainstorms, floods, earthquakes, etc.) that commonly occur in the form of clusters (e.g., Victoriano et al., 2016; Marc et al., 2019; Bessette-Kirton et al., 2020; Abancó et al., 2021; Feng et al., 2024). Hence, they are often utilized for the preliminary analysis regarding the causes and consequences. Additionally, the predictive studies under different future scenarios based on this kind of inventory have also been observed in the literature (Shu et al., 2019; Hürlimann et al., 2022), among which the temporal probability analysis of triggering events was incorporated in most cases. Benefit from the collection of geohazards and scientific knowledge over time, the geohazard databases have been gradually completed at various scales. For example, several well-known studies proposed geohazard inventories worldwide (Froude & Petley, 2018; Kirschbaum et al., 2010), which widely improved insights for geohazard distribution, risk characteristics, and early warning methods from the scientific community (Jia et al., 2020). Geohazard database for countries have been also developed, including but not limited to Europe (Görüm & Fidan, 2021; Haque et al., 2016; Taylor et al., 2015), East Asia (Lin & Wang, 2018; Zhang et al., 2023), and South American (Garcia-Delgado et al., 2022). Among these studies, remote sensing (Jaboyedoff et al., 2012), field survey, and Geostatistics (Medina et al., 2021) are the most widely applied techniques.

Understanding the exact spatial and temporal distribution of geohazards would enable a better understanding of the mechanisms and conditioning factors, as well as avoiding and mitigating the damage caused by these disasters (Görüm & Fidan, 2021; Shao et al., 2022; Zhuang et al., 2018). Regarding this topic, GIS-based landslide susceptibility and risk assessment are a common analysis procedure, where data-driven models have been widely reported and applied in the literature (Reichenbach et al., 2018; Guo et al., 2023). For instance, Chang et al. (2023) developed efficient and automatic multi-scale segmentation method of slope units, combined with the heterogeneity of conditioning factors for landslide susceptibility mapping. It achieved a more accurate spatial assessment of landslides, and had important reference significance for land use and geohazard prevention. However, most of the studies consider the landslide inventory as an entire group, without the analysis of landslide typology. Only limited attempts have been made to distinguish the impacts of slope failure patterns on the occurrence probability under extreme conditions (Zêzere, 2002; Shu et al., 2021). Hence, it is an urgent task to improve the inventory and temporal-spatial characteristics of the geohazards induced by a specific factor. In particular, more attention should be paid to the regions subject to special geological or climate conditions (Crozier, 2010; Cui et al., 2022). In these regions, geohazards will happen repeatedly due to the triggering events beyond a specific exceedance probability. For example, the region in the active fault zones suffers from earthquake-induced geohazards (Lahusen et al., 2020; Zhao et al., 2023). As a country with complex topography and geomorphology country, China often suffers from various geohazards, which have caused considerable losses (Tang et al., 2019; Guo et al., 2020b). Hence, it is important to update more case studies of hotspots to provide the latest insights on this topic. Additionally, subject to data availability, the aforementioned studies mainly focused on the sole aspect of temporal or spatial distribution characteristics, and few of them performed a comprehensive analysis with regard to both. Zeng et al. (2024) integrated ensemble learning and MT-InSAR to enhance the susceptibility zonation of slow-moving landslides in reservoir areas. It was a strong improvement for the tempo-spatial coupled prediction for geohazards. In addition, the land use factor was commonly ignored during the analysis, while it played an important role in the occurrence of geohazards in heavily vegetated areas.

The main objective of the present study is to analyze and reveal the distribution and temporal-spatial characteristics of geohazards at the regional scale, because it is considered a foundational task for hazard assessment and risk management. The Wenzhou City of Zhejiang Province in SE China was taken as a study area, which often suffers from monsoon and rainstorm events in summer. Specific aims include: (i) construction of the database incorporating geohazards during the past two decades (from 2004 to 2023), (ii) analysis of the relationship between different types of geohazards and rainfall, and (iii) determination of distribution characteristics of geohazards associated with environmental factors and administrative areas. Herein, the so-called geohazards only take three types into account, namely landslide, debris flow, and collapse, since they are the most frequent in the study area and have evidently higher risks to residents than others.

## 2. Study Area

### 2.1. General settings

The study area is Wenzhou City, Zhejiang Province (SE China), approximately 300 km southeast of Hangzhou, the capital city of Zhejiang (Fig. 1A). The coordinate is between 27°03' and 28°36' N, 119°37' and 121°18' E, with a total area is 12,083 km$^2$. The study area is part of the Feiyun River, which flows into the Pacific Ocean. The highest peak of the region is 1700 m ASL, thus indicating the elevation difference in the study area is more than 1600 m. The general topography in the area is lower in the east and higher in the west, and the physiography in the western part is characterized as rugged, which has been eroded and dissected to form gorges. The rugged physiography is a result of various tectonic movements and erosional processes. Meanwhile, the steep mountainous areas also often cause various mass movements, such as rockfall, sliding, toppling, rotational failures, and associated other landslides. The highway section that crosses through this region is repeatedly obstructed and damaged by different slope failures during the rainy season. Geologically, the most important lithology in the area is the Volcanic Rock, and the outcrops also include the sedimentary rocks, mainly from the early Cretaceous Period.

The water sources in the area are rich, and most of the seasonal and perennial streams that drain the area originate from the Feiyun River and are characterized by the dendritic to sub-parallel drainage patterns. Regarding the society and population, there are a total of 12 administrative areas (second-level administrative scale) in the study area, and the residents reach 9 million, which represents a density of 700 people/km$^2$.

### 2.2. Rainfall regime

Due to the location close to the Pacific Ocean, the study area has an evident monsoon humid climate, which is mainly characterized by abundant precipitation and four distinct seasons. To characterize the regional rainfall regime, the rainfall time series during the past decades (1960–2020) at the rain gauge were collected from Resource and Environment Science Data Platform RESDP (2024), and the rainstorm information was obtained from the local meteorological authority. As seen in Fig. 1B and Fig. 1C, the average annual rainfall of the region is between 1200 and 2100 mm, and the western part (hill and mountainous areas) has a higher rainfall than that of the eastern part (coastal area). The rainfall regime has an evident temporal difference, and most of the rainfall happens from May to September, which accounts for more than 60% of the annual rainfall. On the contrary, less than 20% of the annual rainfall occurs during the period from October to the next February. For example, the average rainfall for June, July, and August from 1960 to 2020 all exceeds 250 mm, while that for December is less than 50 mm. Moreover, affected by the monsoon over the Pacific Ocean, the study area nearly suffers from several typhoon events on a

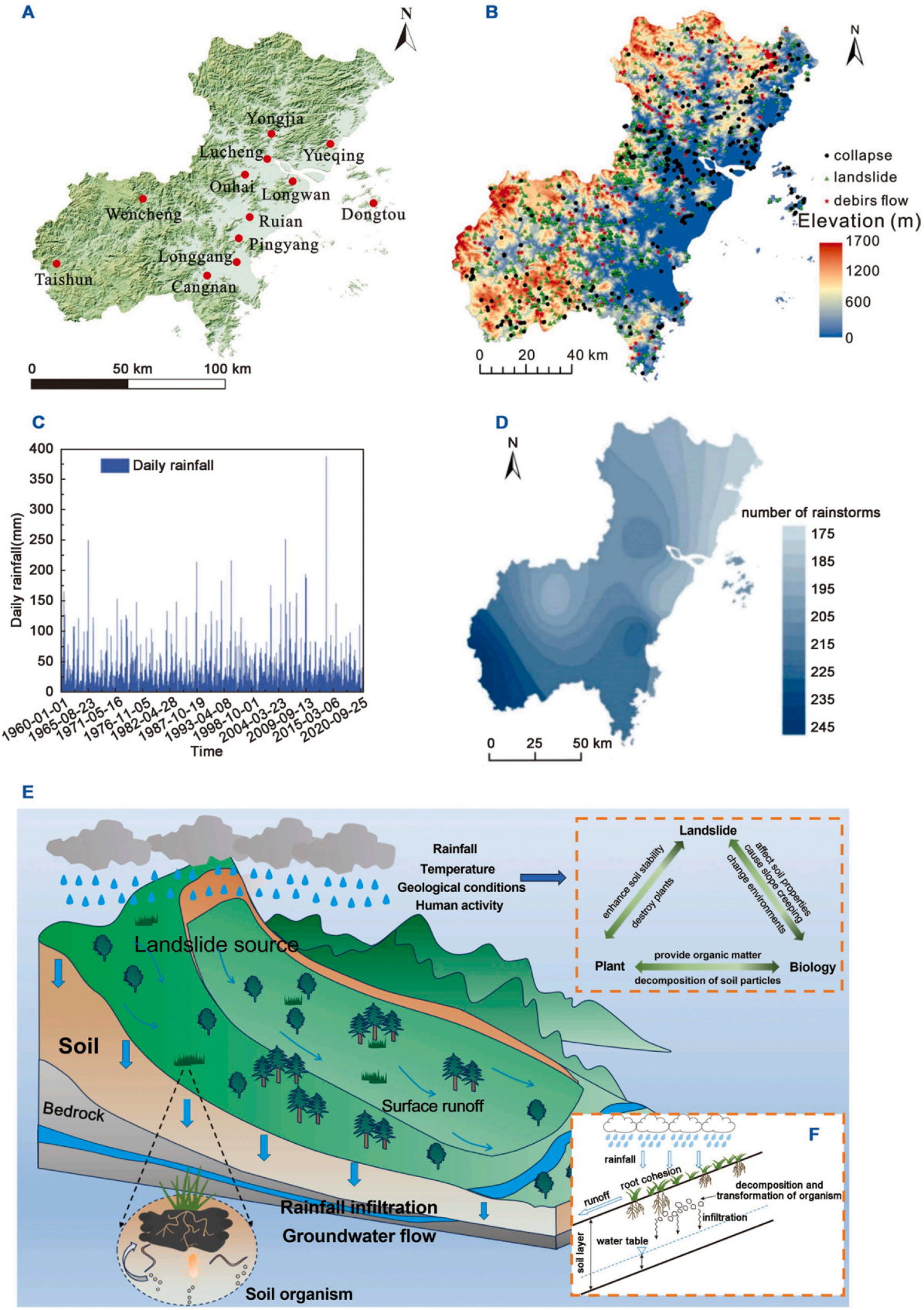



**Fig. 1.** (**A**) Distribution of administration area; (**B**) Spatial distribution of the geohazards in the study area, where the DEM with 30-m resolution was used as the base map; (**C**) Daily rainfall of the study area during 1960 and 2020; (**D**) The average number of days of rainstorm at a yearly basis in the study area; (**E**) The schematic diagram showing the overall relationship among landslide, plant and biology; (**F**) The general effects of plants and biology on slopes under rainfall scenarios.

yearly basis, which bring with them rainstorms. Hence, the average days of rainstorms in the region can reach half of a year or even more.

## 3. Data and methods

### 3.1. Data sources and geohazard inventorying

To construct the regional geohazard database for subsequent analysis, multi-source data were obtained and integrated, including: (i) the historical geohazard catalog provided by the local geological and environmental monitoring administration, which mainly includes the geohazards determined by normal field survey and engineering investigation. (ii) The geohazards induced by specific rainstorms, especially typhoon events. Subject to the spatial characteristics of triggering events, these geohazards are commonly in a cluster. (iii) The archived report for single geohazards that occurred sporadically. Subsequently, the field survey and manual cross-check were conducted to determine the final database. It should be mentioned that, considering the accuracy of geohazards associated with the data long time ago is not satisfactory, so the geohazards during the past two decades were filtered in this study. The collected rainfall dataset had a longer duration (Section 2.2) since it could provide more comprehensive information regarding the regional rainfall regime, which didn't affect the analysis of the relationship between geohazards and rainfall. All the geohazards were projected onto the GIS platform according to their coordinates. Meanwhile, relative information was also linked to the attribute table, such as typology, volume, damages, etc., which allowed for easy statistics.

A total of 1725 geohazards were revealed in this database. which were classified into three types: (i) Landslides: evident displacements along a rupture surface, with the materials of deposits or topsoil covering bedrocks or non-weathered soil layer. (ii) Debris flow: rapid surging flow of saturated debris in a steep channel, and strong entrainment of material and water from the flow path; (iii) Collapse: Sliding of a rock mass on an irregular rupture surface consisting of a number of randomly oriented joints, separated by segments of intact rock (also known as "rock bridge"). Their numbers were 1070, 328, and 327, respectively (Fig. 1D). It should be noted that the aforementioned classification not only referred to related literature (Hungr et al., 2014; Martinello et al., 2024), but also fit with the geohazard prevention practices in China (Yin, 2011). Some types (debris flow and collapse) followed the definitions in the widely accepted criterion (i.e., Hungr et al. (2014)), such as debris flow and collapse, but the so-called "landslide" included a more specific concept than the standard classification. Among these landslides, colluvial landslides, rockslides, and complex landslides were all involved, but these minor classifications were not presented individually, considering the conciseness of the inventory.

The triggering mechanisms for these geohazards were all recorded in the archived reports or forms when they occurred or were investigated. It can be found that most of them were induced by rainfall (see Results section for more details). Moreover, the mountainous area within the region is covered by dense vegetation, so it can be expected that plants and biology play important roles in the landslide mechanism (Fig. 1E,F). The root cohesion of vegetation can enhance the overall slope stability, but some studies also investigated and reported negative effects of vegetation (e.g., Beguería, 2006). From the perspective of mechanics, vegetation gradually reaches a higher suction range near residual water content or wilting point, which will decrease the slope stability (Bordoloi & Ng, 2020). Meanwhile, the hydrological effects of vegetation on slope stability should also not be ignored, especially when involving uncertainties (Guo et al., 2024b). Besides, biology in soil/bedrock layers and soil particles also affects landslides: (i) Rainfall can supply nutrients to organisms decomposing organic matrix in the soil particles, reducing the strength of the layers on which the failure surface forms (Zhang & Mcsaveney, 2018). (ii) Root reinforcement and changes to soil properties introduced by vegetation recovery and biocemented soil, can provoke the redistribution of soil moisture in hillslopes after rainfall (Xiao et al., 2022; Xu et al., 2024). Moreover, slope failures will in turn influence/destroy the living environments of plants and biology. Hence, the relationship between landslide distribution and external environments in the study area should be further investigated in deep.

### 3.2. Influencing factors

Next, important influencing factors in the region were obtained based on a GIS platform to analyze the relationship between geohazards and the factors. The factors mainly included two types, namely topographical (Fig. 2A, B) and geological factors (Fig. 2C–E). Among them, the normalized difference vegetation index (NDVI) was not taken into account, as it presented a high correlation with the land use factor. Additionally, the values of NDVI only reflected the relative abundance of land cover, without strict correspondence to land use types. For the slope map, it can be found that the steep mountains of the region are mainly located in the southwestern part, whereas the eastern part has an average slope angle of less than 10 degrees. Regarding the lithology, glutenite, granite, and pyroclastic rock are the most important types, accounting for more than 70% of the total area. For the land use and land cover (LULC), the study area also presents obvious spatial differences. Forest covers most of the area in the west, and the eastern part is mainly an urban area and farmland.

The soil map used in this study was classified according to the Chinese soil Taxonomy (Gerasimova, 2010; Liu et al., 2020), among which red earths, yellow red earths, yellow earths, and paddy soils are the most important types. These soil types vary in the occurrence mechanism, including sources, pedogenesis, soil fertility, soil texture, material composition, and microorganisms. More details can be found in the Soil Science Database (http://vdb3.soil.csdb.cn/) released by the Institute of Soil Science, CAS.

### 3.3. Landslide susceptibility mapping

Landslide susceptibility mapping can reveal the spatial distribution of landslide-prone areas, thus providing useful information for landslide risk reduction. In this study, the landslide susceptibility map was only used as an assistant way to presenting the areas that have post high landslide risks according to historical events. An approach integrating frequency ratio (FR) and XGBoost algorithm was applied to generate the landslide susceptibility map in the study area. The FR method is a kind of statistical model that can indicate the nonlinear relationship between landslide occurrence and influencing factors. Given that this method has been widely used in this topic, its details are not listed, which could be found in the literature (e.g., Huang et al., 2023).

The XGBoost model is a kind of machine learning approach based on the Boosting algorithm, applying the classification and regression trees as the basic classifier. It has multiple advantages, such as parallel computation and efficient handling of sparse data (Guo et al., 2025). The loss expression of the XGBoost model can be calculated as follows:

$$l(y_i, \hat{y}_i^{(k-1)} + f_k(x_i) \tag{1}$$

where $i$ is a specific iteration process, $k$ represents the $k$-th iteration. Hence, the objective($O$) function during the $k$-th iteration is:

$$O^k = \sum_{i=1}^{n} l(y_i, \hat{y}_i^{(k-1)} + f_k(x_i)) + \Omega(f_k) \tag{2}$$

where $\Omega(f_k)$ is the regularization term, which is used to avoid overfitting issue. It can be denoted as:

$$\Omega(f_k) = \gamma N + \frac{1}{2}\lambda \|W\|^2 \tag{3}$$

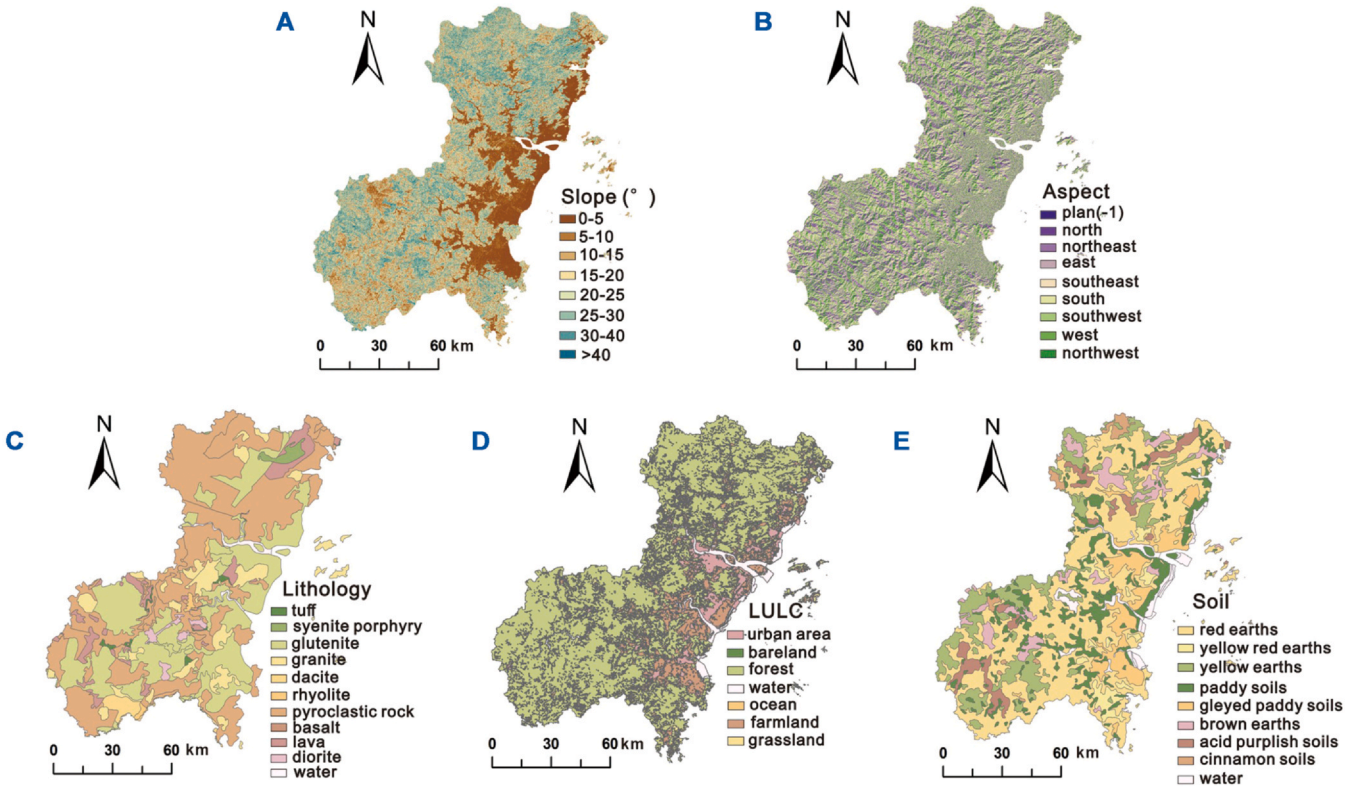



**Fig. 2.** Important factors related to the geohazards: (**A**) Slope; (**B**) Aspect; (**C**) Lithology; (**D**) LULC; (**E**) Soil type.

where $N$ is the total number of leaf nodes, $W$ is the fraction of leaf nodes, $\gamma$ and $\lambda$ are the regularization parameters controlling the complexity of the model. Finally, all the leaf nodes are reclassified to continuously select the single-leaf node with the largest gain. Hence, the objective function of the XGBoost model is calculated as follows:

$$O^k = -\frac{1}{2}\sum_{j=1}^{N}\frac{(\sum_{i\in I_j} g_i)^2}{\sum_{i\in I_j} h_i + \gamma} + \gamma N \tag{4}$$

where $g_i$ and $h_i$ are the first and second order partial derivatives of the loss function, respectively.

## 4. Results and discussion

### 4.1. Basic characteristics of geohazards

Among all the geohazards, the number of landslides was the largest, accounting for 62% of the total, whereas the collapses and debris flows had similar numbers (Fig. 3). Regarding the scale, according to the classification criterion of China Association of Geological Hazard Prevention (CAGHP) (2018), there was 1 large landslide ($10^6$ m$^3$ ≤ volume < $10^7$ m$^3$), 18 medium landslides ($10^5$ m$^3$ ≤ volume < $10^6$ m$^3$), and 1051 small ones (volume < $10^5$ m$^3$), respectively. The damage to properties from the landslides was estimated to be 970 million RMB. This was estimated according to the damages or losses of elements at risk caused by each event and market pricing at the time. The statistical objects included resident properties, farmlands, buildings, and infrastructures. Landslides were mainly distributed in the mountainous areas in the central and southwestern parts of the study area. Regarding the collapses, there were a total of 328 places, accounting for about 19% of the total, and the property threat was estimated to be 230 million RMB. Collapses were mainly distributed in the central and northeastern parts of the region and were relatively small in scale. Among them, there were 2 large collapses ($10^5$ m$^3$ ≤ volume < $10^6$ m$^3$), 10 medium ones ($10^4$ m$^3$ ≤ volume < $10^5$ m$^3$), and 316 small ones (volume < $10^4$ m$^3$). In addition, there were 327 debris flows in the study area, with 35 extremely large hazards (5 × $10^5$ m$^3$ ≤ volume), 33 large ones ($10^5$ m$^3$ ≤ volume < 5 × $10^5$ m$^3$), 76 medium ($10^4$ m$^3$ ≤ volume < $10^5$ m$^3$), and 183 small ones (volume < $10^4$ m$^3$). Property damage caused by mudslides is estimated at 400 million RMB. Generally speaking, debris flows are distributed in all regions in the study area, but more in the northeast and southwest than in the central part, and more inland than along the coast.

According to the materials of the sliding body, the landslides could be classified into three types, namely colluvial landslides, rockslides, and complex type. Their proportions were 52% (colluvial landslide), 4% (rockslide), and 44% (complex), respectively. The colluvial landslides were mainly composed of bedrock weathering crust and residual soil, most of which were characterized as shallow sliding surfaces, with a depth normally less than 2 m; the rest were composed of manual deposits accounting for about 18% of the total. Rockslides normally had a rupture surface following a plane of weakness, such as a bedding plane or a weak layer in the stratigraphy. Most of them were bedding landslides, whereas the rest were nearly horizontal bedding landslides and inverse bedding landslides. The materials of the landslide body were mostly weathered rock mass with a number of randomly oriented joints. The complex type normally consisted of both rock mass and residual soil accumulation, with a complex failure mechanism and often difficult to describe. In addition, different types of landslides present evident differences with respect to scale: most of the colluvial landslides had volumes less than $10^4$ m$^3$ (Fig.3E), while rockslides were larger.

### 4.2. Temporal distribution of geohazards

The distribution of geohazards in each month was analyzed and compared with the average monthly rainfall. As shown in Fig. 4, it can be observed that there are significant temporal distribution differences in all geohazards. The highest number of geohazards occurred from July to September, exceeding 75% of the total number of hazards. For the three types of geohazards, the most frequent occurrences were in

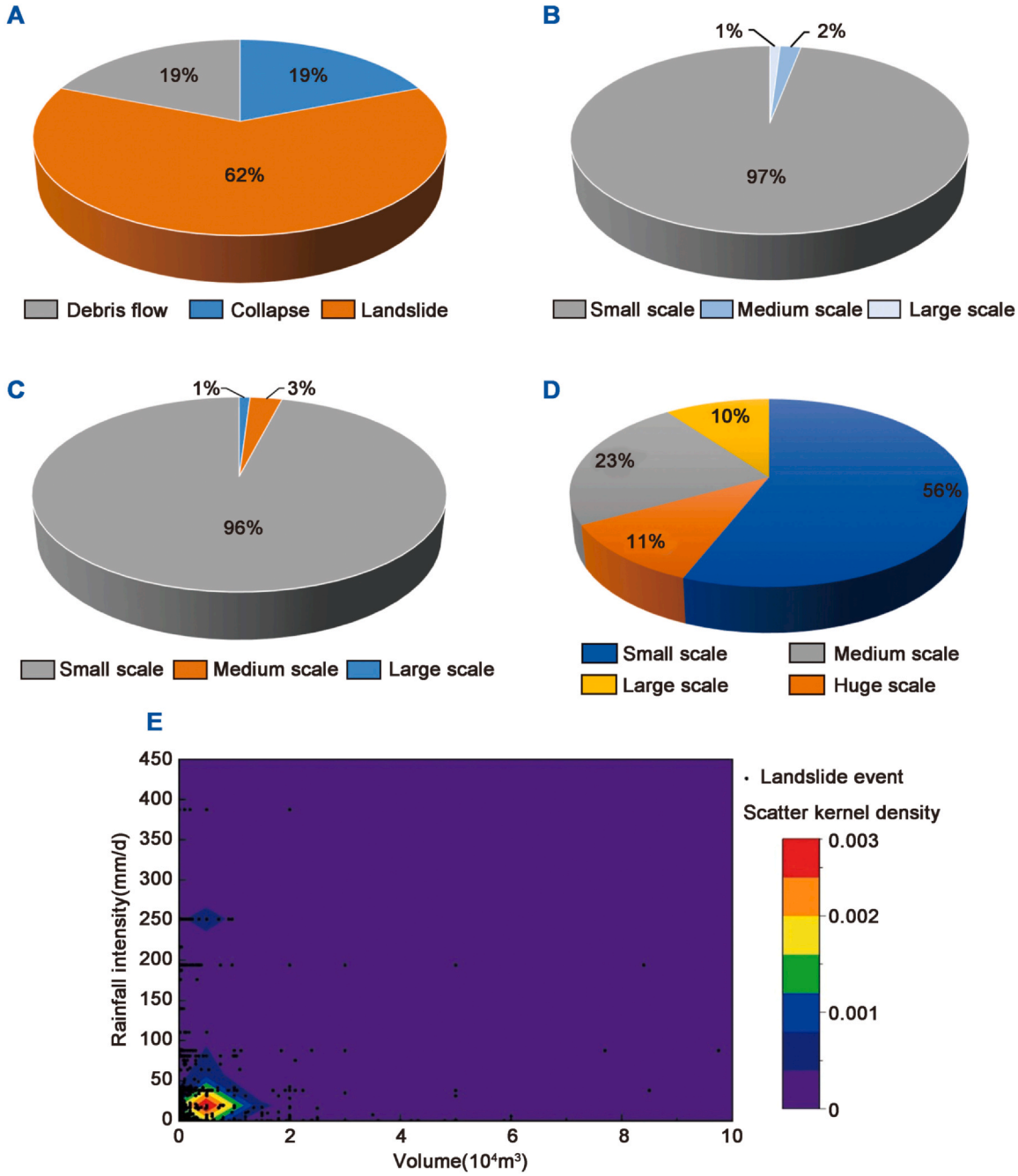



**Fig. 3.** Statistical results of number and scales for different kinds of geohazards: (**A**) Number of various geohazards, (**B**) Scales of landslides, (**C**) scales of collapses, (**D**) Scales of debris flows; (**E**) Relationship between landslide volume and rainfall intensity. The rainfall intensity means the daily rainfall at the date when the landslide event occurred. The volume of each landslide has been indicated in the GIS platform.

August (landslides) and September (collapse, debris flow). During the dry season (November to February of the following year), the number of geohazards significantly decreased, with fewer than 30 occurrences each month. It is interesting that the average rainfall between June and August was similar, while the number of geohazards differed significantly. This is mainly because the antecedent rainfall of June (e.g., the total rainfall of April and May) was evidently smaller than that of August (e.g., the total rainfall of June and July). Recent literature indicated that the landslide initiation condition depended much on antecedent effective recharge (Abraham et al., 2021; Medina et al., 2021).

The aforementioned statistical results lead to the conclusion that there is a high correlation between the temporal distribution of geohazards and rainfall in the study area. This also fits well with the main triggering factors of the geohazards in the region: 55% of the geohazards were induced by typhoon rainstorm events, and 29% of the geohazards were related to non-typhoon rainfall. Only 16% of the geohazards had relationships with other factors except rainfall, including earthquake, engineering activities, and so on.

### 4.3. Spatial distribution of geohazards

#### 4.3.1. Distribution in administration areas

There are a total of 12 administration areas (second-level administrative scale) in the study area, and the distribution of geohazards in each administrative area was accounted for, including quantities and densities. As shown in Fig. 5, it can be found that geohazards were distributed in each administrative region, but there was a significant

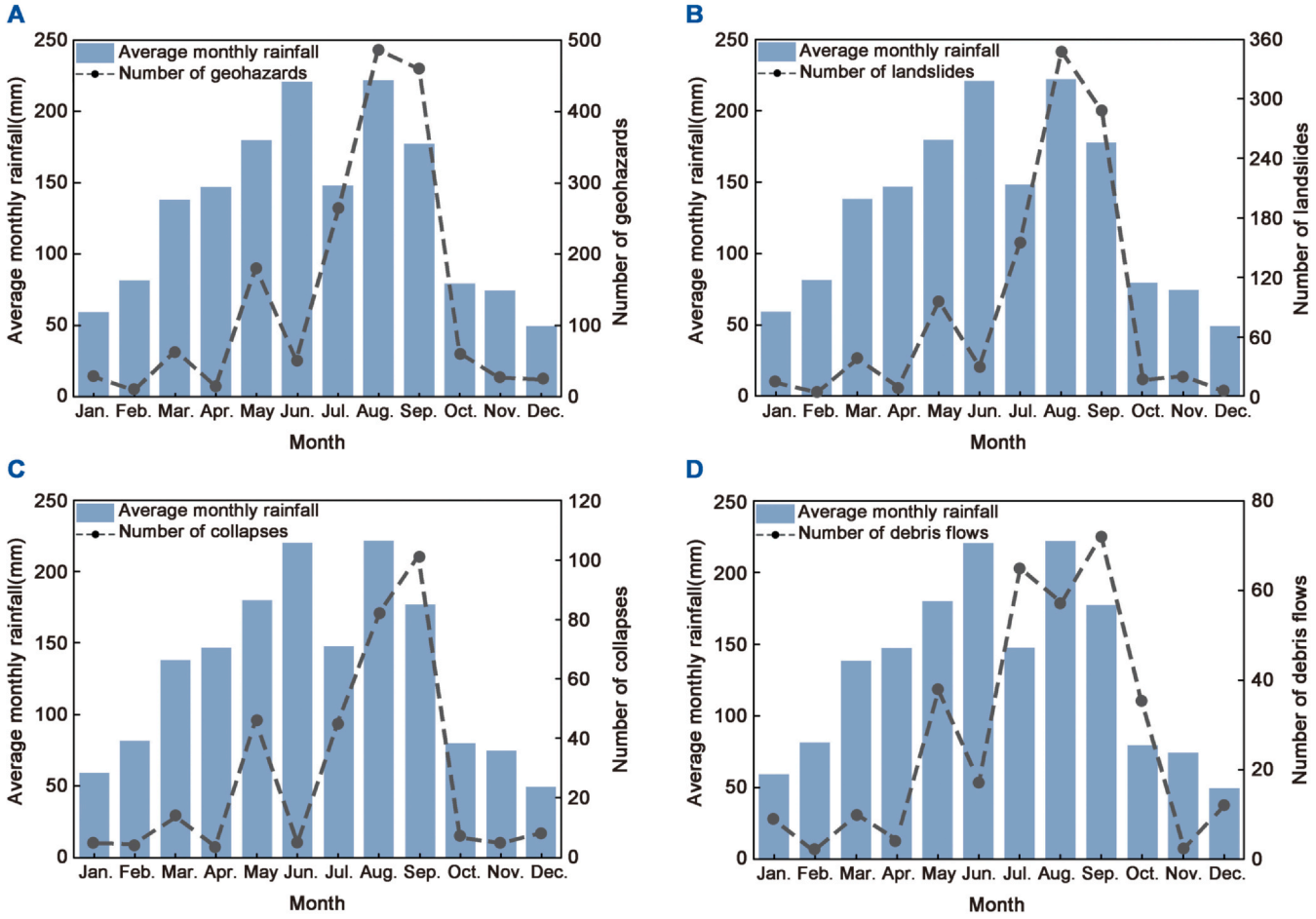



**Fig. 4.** Statistical results of temporal distribution for different kinds of geohazards: **(A)** All of the geohazards; **(B)** Landslides; **(C)** Collapses; **(D)** Debris flows.

uneven distribution. This was mainly related to the factors such as regional topography, geomorphology, and the spatiotemporal distribution of precipitation. The three types of hazards were mainly distributed in the western mountainous areas, including Leqing, Yongjia, Wencheng, Taishun, and Pingyang. On the contrary, the number of geohazards in the eastern coastal areas was significantly lower, such as Dongtou, Longgang, and Longwan. Specifically, the administrative regions with the highest number of individual types of geohazards were Yongjia (landslides, debris flows) and Leqing (collapse), respectively. The peak values of geohazard density appeared in Ouhai (landslides), Lucheng (collapse), and Yueqing (debris flow), respectively.

Next, the landslide susceptibility mapping was conducted based on the FR-XGBoost model and historical events. As seen in Fig. 5E, the general distribution of potential landslides can be observed, which also fits well with the results of the distribution in administrative areas. There are two important landslide-prone regions (very high susceptibility level). One is the northern part of the area (e.g., Yongjia, Leqing, and Ouhai), and the other is the middle-western part (e.g., Pingyang, Wencheng and Taishun).

*4.3.2. Relationship between geohazards and environmental factors*

In order to analyze the spatial distribution characteristics of different types of geohazards and summarize their developmental patterns, the spatial correlations between hazards and various environmental factors, including elevation, slope, soil, and land use, were statistically analyzed. As shown in Fig. 6A–D, the distribution of landslides is closely related to elevation factors, as the environmental conditions of slopes, such as climate and human activities, vary with elevation. The study area has an elevation range of 0–1700 m, which is divided into 8 levels, with each level spanning 200 m. The statistical results show that the majority of landslides occur in mid-low elevation areas, with over 90% of landslides occurring within the elevation range of 0–600 m. As elevation increases, the density of landslides significantly decreases. One possible explanation is that there are more human engineering activities at lower elevations, leading to the triggering of more landslides.

The main function of slope is to change the stability conditions of slope rock and soil, and the surface water dynamic conditions. Statistical results show that landslides mainly occur on slopes between 5 and 30° in the study area, with slopes of 10°–20° having the highest number and point density of landslides, exceeding 250 and 0.12 per $km^2$, respectively. Conversely, for slopes greater than 20°, the landslide density significantly decreases.

Soil type can affect the physical and mechanical properties of soil, such as the size, shape, and density of soil particles, all of which can influence the stability and shear strength of soil. Additionally, soil type can also impact the water characteristics of soil, such as saturation, porosity, and permeability. For the study area, it can be observed that landslides are most numerous when the soil type is red soil, accounting for as high as 65% of landslide points, with a small portion occurring in non-waterlogged paddy soil and brown soil, accounting for 6% of landslide points.

Vegetation has a significant impact on the stability of steep slopes. On one hand, vegetation can increase the risk of instability by making the rock and soil loose through root growth. Under the influence of typhoons, vegetation sways, exacerbating the instability of the rock and soil on steep slopes. On the other hand, under heavy rainfall conditions, loose rock and soil can quickly reach saturation or form transient

| A | Number of geohazards | Area(km²) | Density of geohazards (geohazards/km²) |
|---|---|---|---|
| Cangnan | 153 | 1079.33 | 0.142 |
| Dongtou | 34 | 273.02 | 0.125 |
| Leqing | 208 | 1395.88 | 0.149 |
| Longgang | 4 | 160.4 | 0.025 |
| Longwan | 22 | 316.52 | 0.07 |
| Lucheng | 83 | 292.82 | 0.283 |
| Ouhai | 135 | 466.31 | 0.29 |
| Pingyang | 174 | 1035.68 | 0.168 |
| Ruian | 151 | 1341.61 | 0.113 |
| Tais hun | 256 | 1768.03 | 0.145 |
| Wencheng | 179 | 1296.44 | 0.138 |
| Yongjia | 325 | 2677.65 | 0.121 |

| B | Number of landslides | Area(km²) | Density of landslides (landslides/km²) |
|---|---|---|---|
| Cangnan | 107 | 1079.33 | 0.099 |
| Dongtou | 15 | 273.02 | 0.055 |
| Leqing | 80 | 1395.88 | 0.057 |
| Longgang | 1 | 160.4 | 0.006 |
| Longwan | 11 | 316.52 | 0.035 |
| Lucheng | 50 | 292.82 | 0.171 |
| Ouhai | 84 | 466.31 | 0.180 |
| Pingyang | 155 | 1035.68 | 0.150 |
| Ruian | 100 | 1341.61 | 0.075 |
| Tais hun | 151 | 1768.03 | 0.085 |
| Wencheng | 134 | 1296.44 | 0.103 |
| Yongjia | 181 | 2677.65 | 0.068 |

| C | Number of collapses | Area(km²) | Density of collapses (collapses/km²) |
|---|---|---|---|
| Cangnan | 27 | 1079.33 | 0.025 |
| Dongtou | 18 | 273.02 | 0.066 |
| Leqing | 72 | 1395.88 | 0.052 |
| Longgang | 1 | 160.4 | 0.006 |
| Longwan | 11 | 316.52 | 0.035 |
| Lucheng | 30 | 292.82 | 0.102 |
| Ouhai | 38 | 466.31 | 0.081 |
| Pingyang | 6 | 1035.68 | 0.006 |
| Ruian | 16 | 1341.61 | 0.012 |
| Tais hun | 50 | 1768.03 | 0.028 |
| Wencheng | 12 | 1296.44 | 0.009 |
| Yongjia | 47 | 2677.65 | 0.018 |

| D | Number of debris flows | Area(km²) | Density of debris flows (debris flows/km²) |
|---|---|---|---|
| Cangnan | 19 | 1079.33 | 0.018 |
| Dongtou | 1 | 273.02 | 0.004 |
| Leqing | 56 | 1395.88 | 0.040 |
| Longgang | 2 | 160.4 | 0.012 |
| Longwan | 0 | 316.52 | 0.000 |
| Lucheng | 3 | 292.82 | 0.010 |
| Ouhai | 13 | 466.31 | 0.028 |
| Pingyang | 13 | 1035.68 | 0.013 |
| Ruian | 35 | 1341.61 | 0.026 |
| Tais hun | 55 | 1768.03 | 0.031 |
| Wencheng | 33 | 1296.44 | 0.025 |
| Yongjia | 97 | 2677.65 | 0.036 |

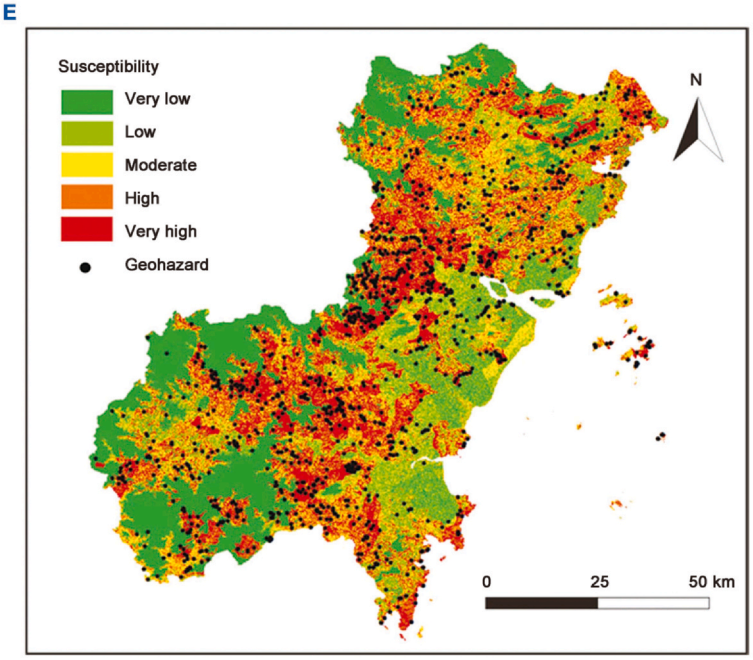



**Fig. 5.** Spatial distribution characteristics of geohazards in different administration areas: **(A)** All of the geohazards, **(B)** Landslides, **(C)** Collapses, **(D)** Debris flows; **(E)** Landslide susceptibility map based on FR-XGBoost model.

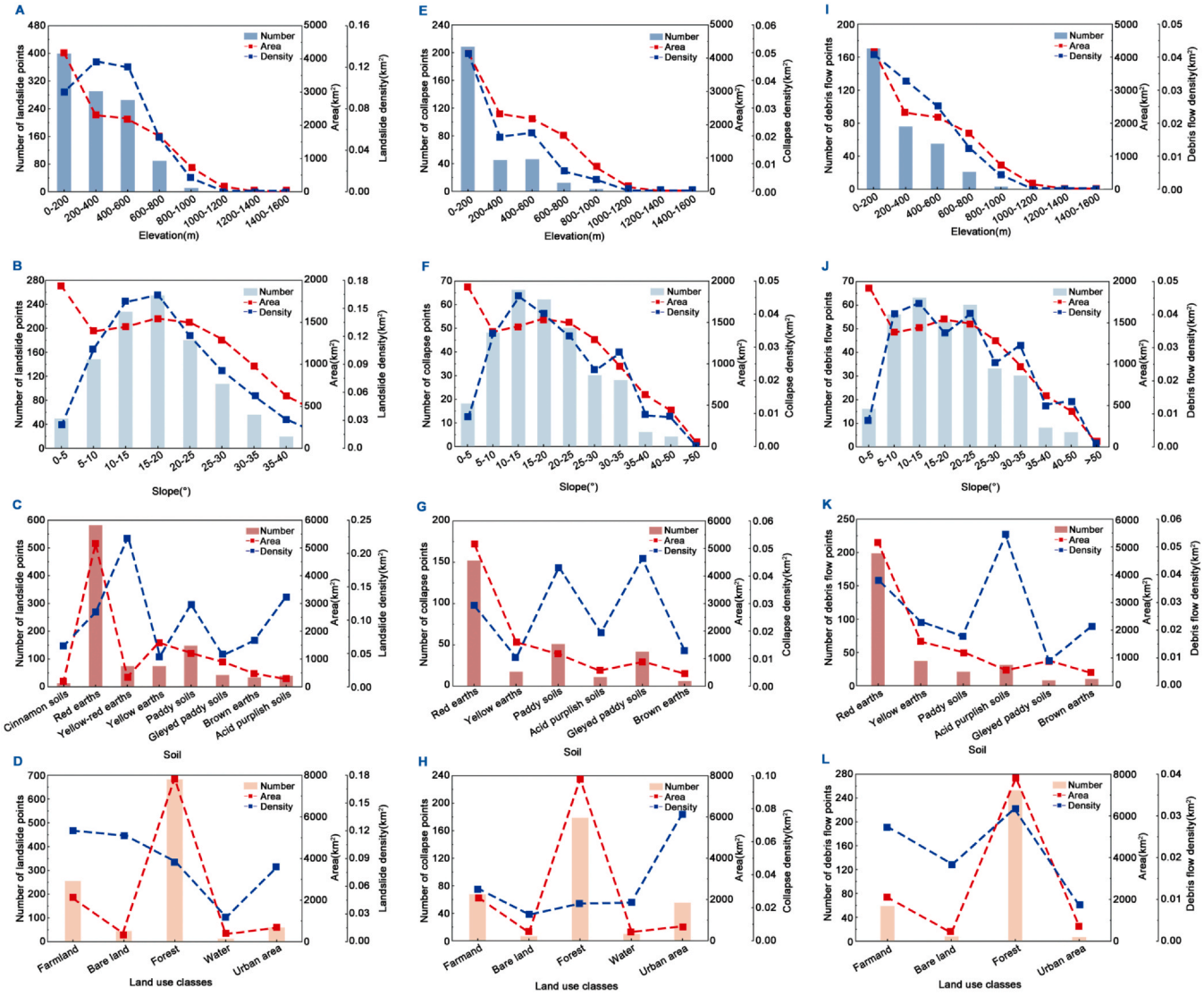



**Fig. 6.** The analysis of different geohazards and the effect of environmental factors, including elevation, slope angle, soil type and land use. **(A–D)** Results regarding the landslides, **(E–H)** Results regarding the collapses, **(I–L)** Results regarding the debris flows

saturation zones, causing all precipitation to convert into runoff in a short period of time. The erosive force of this runoff far exceeds the protective effect of vegetation on the rock and soil of the slope. From Fig. 6D, it can be seen that most landslide points are located in areas with larger forest and cultivated land, with a smaller portion in grasslands and water bodies. However, landslide density data show that cultivated land and grasslands are more prone to landslide events. This may be related to human activities and the interaction of vegetation roots with the soil.

The distribution pattern of collapses under the influence of elevation follows a similar trend to landslides overall, with the highest number of collapse points occurring in the mid-low elevation areas (Fig. 6E–H). Particularly, within the elevation range of 0–200 m, the number of collapse points reaches 208, accounting for 66% of the total collapses. A small portion is located within the 600–1000 m elevation range, with 15 collapse points, accounting for approximately 5%.

Regarding the slope factor, collapses mainly occur on slopes ranging from 5° to 25°, with the majority happening in the 5°–15° slope range. The number and density of collapses increase significantly with the increase in slope within the 5°–15° range. For slopes greater than 15°, the number and density of collapses show a decreasing trend.

The collapse points are mainly distributed in red soil, paddy soil, and dehydrated paddy soil. The number of collapse points in these areas is 245, accounting for 88% of the total. Among them, the highest number of collapse points occurs in red soil, with 152 points, accounting for 54%. Additionally, although the coverage area of paddy soil and dehydrated paddy soil is small, the density of collapses is higher, at 0.043/km$^2$ and 0.047/km$^2$, respectively. When the soil type is brown soil, the fewest collapse points are recorded, with 6 points, accounting for 2%.

When the land use is forested, there are the most collapse points, reaching 178, accounting for 58%. The fewest collapse points are recorded in grasslands and water bodies, with 15 points, accounting for approximately 5%. It is important to note that residential land has the highest collapse density, at 0.077/km$^2$, significantly higher than other types of land use (below 0.003/km$^2$).

Debris flows are also distributed in lower altitude areas (Fig. 6I–L). Within the elevation range of 0–600 m, there are 301 debris flows, accounting for 93% of the total. Among them, the highest number of debris flows occurs in the elevation range of 0–200 m, reaching 170 points, accounting for 52%. The fewest debris flows are found in the elevation range of 800–1000 m, with only 3 points, accounting for 1%.

Debris flows are mainly concentrated on slopes ranging from 5° to 35°, accounting for over 80% of the total debris flows. The probability of debris flows occurring on slopes less than 5° or greater than 35° is relatively low. Within the slope range of 0°–15°, the number and density of debris flows significantly increase with the slope's increase. For slopes greater than 25°, both the number and density of debris flows show a decreasing trend.

More than 65% of the debris flows are distributed in red soil, with a total of 199 points. When the soil type is dehydrated paddy soil, the fewest debris flows are recorded, with only 8 points. Another significant feature is the significantly higher density for the debris flows observed in acidic soil compared to other soil types, reaching 0.055/km$^2$.

Similar to landslides and collapses, debris flows are mainly distributed in the forested areas, with 252 points accounting for 78% and a point density of 0.032 per km$^2$. Additionally, significant debris flow densities are observed in the farmland. The fewest debris flow points are found in urban and rural industrial and residential land, totaling 6 points and accounting for 2%.

### 4.4. Limitations and policy recommendations

While the present study had a relatively comprehensive database, the time span was not satisfactory. Given the data availability and accuracy, only the geohazards during the past two decades were filtered. It is evident that with the development of technology, the datasets from the most recent are more accurate than those from a long time ago. This requires users to update the current data continuously, with the premise that the multisource heterogeneous data should be limited. Moreover, it has been noticed that the database established in this study differed from those existing in the literature (e.g., Dou et al., 2023; Zhang et al., 2023). This highlights an open issue in the geohazard prevention practices in China, namely, regional standards and systematic databases are normally not available. In fact, China has its own national criteria regarding geohazards, which are different from the widely used international definition. Hence, it is more complex to establish and describe a geohazard database, especially at large scales. This may raise concerns that the consistency of the standard and the results are too “local”, since they are difficult to duplicate in other settings for comparison.

While the present analysis showed the statistical relationship between geohazards and land use, a detailed analysis of the vegetation effect of the landslides was not conducted. This is a complex topic since both hydrological and mechanical aspects should be considered meanwhile. As Bordoloi and Ng (2020) stated, vegetation commonly has a “love–hate relationship” with slope stability. Most studies think plants can improve slope stability through root cohesion (Lan et al., 2020; Hürlimann et al., 2022), hence the areas with dense forests and shrubs are normally observed with low-density geohazards. However, some studies (including this study) also reported opposite results (e.g., Shu et al., 2019). This indicates that the vegetation effects could also be destabilization for slopes, such as through changing topography and soil hydrological characteristics. Hence, one of the future works could focus on revealing specific vegetation effects on geohazards using laboratory tests and numerical simulations. In fact, some related techniques on this topic have been developed (Ni et al., 2018; Ng et al., 2022), which may be of high interest to the science community.

Last but not least, current results indicate that densely vegetated regions may pose higher geohazard risk under rainstorm scenarios. However, the inventories based on optical imagery or photographs are normally incomplete in heavily vegetated areas. Evidently, more field surveys should be performed to complete event-based geohazard inventories. Meanwhile, given the limitations of applications of the InSAR technique in such settings, early warning systems may be quite necessary in some potential geohazard sites. It has been noticed that some urban areas are still located in high geohazard-prone zones. it is therefore an urgent task to implement comprehensive risk assessments and corresponding mitigation measures.

## 5. Conclusion

Due to the influence of hilly terrain and temperate monsoon climate, the coastal areas in southeastern China often suffer from geohazards during the rainy season, resulting in widespread casualties and property losses. Therefore, a detailed analysis of the spatiotemporal characteristics of geohazards needs to be conducted. Based on the analysis of multiple data sources, this study has constructed a geohazard database for Wenzhou City (SE China) over the past 20 years. The database reveals 1725 geohazards, including 1070 landslides, 328 collapses, and 327 debris flows. These hazards have caused total economic losses exceeding 1.5 billion RMB. The triggering factors of these disasters mainly fall into three categories: typhoon-induced heavy rainfall, non-typhoon rainfall, and non-rainfall. The proportions of geohazards triggered by different factors are 55%, 29%, and 16%, respectively. In terms of temporal distribution, the majority of geohazards show a strong correlation with monthly rainfall, with over 70% of geohazards occurring between May and September, while the fewest ones occur from November to February of the following year. The correlation between geohazards and the distribution of administrative regions also varies significantly, with more geohazards occurring in the mountainous areas in the western part of the study area, indicating a higher geohazard risk. Conversely, the number and density of disasters in the eastern coastal areas are significantly lower. Similar spatial differences are observed in different environmental factors: most geohazards occur in areas with lower elevation (0–600 m ASL), moderate slope (0–25 degrees), and forest cover. The research results mentioned above can provide an important theoretical basis for geohazard risk management and mitigation in this region.

## CRediT authorship contribution statement

**Lu Shi:** Investigation. **Zhanxu Guo:** Validation. **Luqi Wang:** Methodology. **Yuhua Zhang:** Data curation. **Zizheng Guo:** Formal analysis. **Guangqi Chen:** Supervision. **Mengchen Cheng:** Writing – original draft. **Haojie Wang:** Validation. **Xinyong Zhou:** Software.

## Declaration of Competing Interest

The authors declare that they have no known competing financial interests or personal relationships that could have appeared to influence the work reported in this paper.

## Acknowledgements

This research is funded by the National Natural Science Foundation of China (No.42307248), Hebei Province Full-Time Introduction of High-End Talent Research Project Funding, and China Postdoctoral Foundation (2024M753842).

## References

Abancó, C., Bennett, G. L., Matthews, A. J., Matera, M. A. M., & Tan, F. J. (2021). The role of geomorphology, rainfall and soil moisture in the occurrence of landslides triggered by 2018 Typhoon Mangkhut in the Philippines. *Natural Hazards And Earth System Sciences, 21*(5), 1531–1550. https://doi.org/10.1016/j.catena.2021.105147

Abraham, M. T., Satyam, N., Rosi, A., Pradhan, B., & Segoni, S. (2021). Usage of antecedent soil moisture for improving the performance of rainfall thresholds for landslide early warning. *Catena, 200*, 105147. https://doi.org/10.1016/j.catena.2021.105147

Bessette-Kirton, E. K., Coe, J. A., Schulz, W. H., Cerovski-Darriau, C., & Einbund, M. M. (2020). Mobility characteristics of debris slides and flows triggered by Hurricane Maria in Puerto Rico. *Landslides, 17*, 2795–2809. https://doi.org/10.1007/s10346-020-01445-z

Beguería, S. (2006). Changes in land cover and shallow landslide activity: a case study in the Spanish Pyrenees. *Geomorphology, 74*, 196–206. https://doi.org/10.1016/j.geomorph.2005.07.018

Bordoloi, S., & Ng, C. W. W. (2020). The effects of vegetation traits and their stability functions in bio-engineered slopes: A perspective review. *Engineering Geology, 275*, 105472. https://doi.org/10.1016/j.enggeo.2020.105742

Chang, Z., Catani, F., Huang, F., Liu, G., Meena, S. R., Huang, J., & Zhou, C. (2023). Landslide susceptibility prediction using slope unit-based machine learning models considering the heterogeneity of conditioning factors. *Journal of Rock Mechanics and Geotechnical Engineering, 15*(5), 1127–1143. https://doi.org/10.1016/j.jrmge.2022.07.009

China Association of Geological Hazard Prevention (CAGHP). Standard of Classification for Geological Hazards. 2018 (in Chinese). Last accessed 20 December 2024. 〈https://std.cgs.gov.cn/content/678〉.

Crozier, M. J. (2010). Deciphering the effect of climate change on landslide activity: a review. *Geomorphology, 124*(3–4), 260–267. https://doi.org/10.1016/j.geomorph.2010.04.009

Cui, P., Ge, Y., Li, S., et al. (2022). Scientific challenges in disaster risk reduction for the Sichuan–Tibet Railway. *Engineering Geology, 309*, 106837. https://doi.org/10.1016/j.enggeo.2022.106837

Dou, H., Wan, R., an, & Jian, H. (2023). W. Rainfall early warning threshold and its spatial distribution of rainfall-induced landslides in China. *Rock Mechanics Bulletin, 2*(3), 100156. https://doi.org/10.1016/j.rockmb.2023.100056

Feng, P., Li, C., Zhang, S., Meng, J., & Long, J. (2024). Integrating Shipborne Images with Multichannel Deep Learning for Landslide Detection. *Journal of Earth Science, 35*(1), 296–300. https://doi.org/10.1007/s12583-023-1957-5

Froude, M. J., & Petley, D. N. (2018). Global fatal landslide occurrence from 2004 to 2016. *Natural Hazards and Earth System Sciecnes, 18*, 2161–2181. https://doi.org/10.5194/nhess-18-2161-2018

Garcia-Delgado, H., Petley, D. N., Bermúdez, M. A., & Sepúlveda, S. A. (2022). Fatal landslides in Colombia (from historical times to 2020) and their socio-economic impacts. *Landslides, 19*, 1689–1716. https://doi.org/10.1007/s10346-022-01870-2

Gerasimova, M. I. (2010). Chinese soil taxonomy: Between the American and the international classification systems. *Eurasian Soil Science, 43*, 945–949. https://doi.org/10.1134/S1064229310080120

Guo, Z., Chen, L., Yin, K., Shrestha, D. P., & Zhang, L. (2020a). Quantitative risk assessment of slow-moving landslides from the viewpoint of decision-making: A case study of the Three Gorges Reservoir in China. *Engineering Geology, 273*, Article 105667.

Guo, Z., Chen, L., Gui, L., Du, J., Yin, K., & Do, H. M. (2020b). Landslide displacement prediction based on variational mode decomposition and WA-GWO-BP model. *Landslides, 17*, 567–583.

Guo, Z., Tian, B., He, J., Xu, C., Zeng, T., & Zhu, Y. (2023). Hazard assessment for regional typhoon-triggered landslides by using physically-based model -A case study from southeastern China. *Georisk: Assessment and Management of Risk for Engineered Systems and Geohazards, 17*(4), 740–754. https://doi.org/10.1080/17499518.2023.2188465

Guo, Z., Wang, H., He, J., Huang, D., Song, Y., Wang, T., ... Ferrer, J. V. (2025). PSLSA v2.0: An automatic Python package integrating machine learning models for regional landslide susceptibility assessment. *Environmental Modelling Software, 186*, 106367. https://doi.org/10.1016/j.envsoft.2025.106367

Guo, Z., Zhou, X., Huang, D., Zhai, S., & Tian, B. (2024a). Dynamic simulation insights into friction weakening effect on rapid long-runout landslides: a case study of the yigong landslide in the Tibetan Plateau, China. *China Geology, 7*(2), 222–236.

Görüm, T., & Fidan, S. (2021). Spatiotemporal variations of fatal landslides in Turkey. *Landslides, 18*, 1691–1705. https://doi.org/10.1007/s10346-020-01580-7

Guo, H., Qu, C., Liu, L., Zhang, Q., & Liu, Y. (2024b). Reliability analysis of vegetated slope considering spatial variability of soil and root properties. *Computers and Getechnics, 169*, Article 106257.

Guzzetti, F., Mondini, A. C., Cardinali, M., Fiorucci, F., Santangelo, M., & Chang, K. T. (2012). Landslide inventory maps: New tools for an old problem. *Earth-Science Reviews, 112*(1–2), 42–66. https://doi.org/10.1016/j.earscirev.2012.02.001

Haque, U., Blum, P., & da Sliva, P.F., et al. (2016). Fatal Landslides in. Europe, 13, 1545–1554. https://doi.org/10.1007/s10346-016-0689-3.

Huang, F., Teng, Z., Guo, Z., Catani, F., & Huang, J. (2023). Uncertainties of landslide susceptibility prediction: Influences of different spatial resolutions, machine learning models and proportions of training and testing dataset. *Rock Mechanics Bulletin, 2*(1), Article 100028. https://doi.org/10.1016/j.rockmb.2023.100028

Hungr, O., Leroueil, S., & Picarelli, L. (2014). The Varnes classification of landslide types, an update. *Landslides, 11*(2), 167–194. https://doi.org/10.1007/s10346-013-0436-y

Hürlimann, M., Guo, Z. Z., Puig-Polo, C., & Medina, V. (2022). Impacts of future climate and land cover changes on landslide susceptibility: regional scale modelling in the Val d'Aran region (Pyrenees, Spain). *Landslides, 19*(1), 99–118. https://doi.org/10.1007/s10346-021-01775-6

Jaboyedoff, M., Oppikofer, T., Abellán, A., Derron, M. H., Loye, A., Metzger, R., & Pedrazzini, A. (2012). Use of LIDAR in landslide investigations: a review. *Natural hazards, 61*, 5–28. https://doi.org/10.1007/s11069-010-9634-2

Jia, G., Tang, Q., & Xu, X. (2020). Evaluating the performances of satellite-based rainfall data for global rainfall-induced landslide warnings. *Landslides, 17*, 283–299. https://doi.org/10.1007/s10346-019-01277-6

Kamran, M., Hu, X., Hussain, M. A., Sanaullah, M., Ali, R., & He, K. (2023). Dynamic Response and Deformation Behavior of Kadui-2 Landslide Influenced by Reservoir Impoundment and Rainfall, Baoxing, China. *Journal of Earth Science, 34*(3), 911–923. https://doi.org/10.1007/s12583-022-1649-6

Kirschbaum, D. B., Adler, R. F., Hong, Y., Hill, S., & Lerner-Lam, A. (2010). A global landslide catalog for hazard applications: method, results, and limitations. *Natural Hazards, 52*, 561–575. https://doi.org/10.1007/s11069-009-9401-4

Lahusen, S. R., Duvall, A. R., Booth, A. M., Grant, A., Mishkin, B. A., Montgomery, D. R., ... Wartman, J. (2020). Rainfall triggers more deep-seated landslides than Cascadia earthquakes in the Oregon Coast Range, USA. *Science Advances, 6*(38), eaba6790. https://doi.org/10.1126/sciadv.aba6790

Lan, H., Wang, D., He, S., Fang, Y., Chen, W., Zhao, P., & Qi, Y. (2020). Experimental study on the effects of tree planting on slope stability. *Landslides, 17*, 1021–1035. https://doi.org/10.1007/s10346-020-01348-z

Li, W., & Huang, Y. (2023). Model tests on the effect of dip angles on flow behavior of liquefied sand. *Journal of Earth Science, 34*, 381–385. https://doi.org/10.1007/s12583-021-1498-8

Lin, Q., & Wang, Y. (2018). Spatial and temporal analysis of a fatal landslide inventory in China from 1950 to 2016. *Landslides, 15*, 2357–2372. https://doi.org/10.1007/s10346-018-1037-6

Liu, F., Zhang, G., Song, X., Le, D., Zhao, Y., Yang, J., ... Yang, F. (2020). High-resolution and three-dimensional mapping of soil texture of China. *Geoderma, 361*, 114061. https://doi.org/10.1016/j.geoderma.2019.114061

Marc, O., Gosset, M., Saito, H., Uchida, T., & Malet, J. P. (2019). Spatial Patterns of Storm-Induced Landslides and Their Relation to Rainfall Anomaly Maps. *Geophysical Research Lettes, 46*(20), 11167–11177. https://doi.org/10.1029/2019GL083173

Martinello, C., Delchiaro, M., Iacobucci, G., Cappadonia, C., Rotigliano, E., & Piacentini, D. (2024). Exploring the geomorphological adequacy of the landslide susceptibility maps: A test for different types of landslides in the Bidente river basin (northern Italy). *Catena, 238*, 107835. https://doi.org/10.1016/j.catena.2024.107835

Medina, V., Hürlimann, M., Guo, Z., Lloret, A., & Vaunat, J. (2021). Fast physically-based model for rainfall-induced landslide susceptibility assessment at regional scale. *Catena, 201*, 105213. https://doi.org/10.1016/j.catena.2021.105213

Ng, C. W. W., Qu, C., Ni, J., & Guo, H. (2022). Three-dimensional reliability analysis of unsaturated soil slope considering permeability rotated anisotropy random fields. *Computers and Geotechnics, 151*, 104944. https://doi.org/10.1016/j.compgeo.2022.104944

Ng, C. W. W., Qu, C., Guo, H., Chen, R., & Xue, Q. (2024). Probabilistic analysis of a sustainable landfill cover considering stress-dependent water retention model and copula-based random fields. *Engineering Geology, 332*, 107460. https://doi.org/10.1016/j.enggeo.2024.107460

Ni, J. J., Leung, A. K., Ng, C. W. W., & Shao, W. (2018). Modelling hydro-mechanical reinforcements of plants to slope stability. *Computers and Geotechnics, 95*, 99–109. https://doi.org/10.1016/j.compgeo.2017.09.001

Ouyang, C., Zhao, W., Xu, Q., Peng, D., Li, W., Wang, D., ... Hou, S. (2018). Failure mechanisms and characteristics of the 2016 catastrophic rockslide at Su village, Lishui, China. *Landslides, 15*, 1391–1400. https://doi.org/10.1007/s10346-018-0985-1

Petley, D. N. (2012). Global patterns of loss of life from landslides. *Geology, 40*, 927–930. https://doi.org/10.1130/G33217.1

Qin, H., He, J., Guo, J., & Cai, L. (2022). Developmental characteristics of rainfall-induced landslides from 1999 to 2016 in Wenzhou City of China. *Frontiers in Earth Science, 10*, 1005199. https://doi.org/10.3389/feart.2022.1005199

Reichenbach, P., Rossi, M., Malamud, B. D., Mihir, M., & Guzzetti, F. (2018). A review of statistically-based landslide susceptibility models. *Earth-Science Reviews, 180*, 60–91. https://doi.org/10.1016/j.earscirev.2018.03.001

Resource and Environment Science Data Platform (RESDP), Last accessed 20 December 2024. 〈https://www.resdc.cn/〉.

Shao, C., Lu, Y., Lan, H., Li, L., Liu, S., Yan, Z., & Li, Y. (2022). Spatiotemporal distribution characteristics, causes, and prevention advice of fatal geohazards in Jiangxi Province, China. *Science of The Total Environment, 834*, 155337. https://doi.org/10.1016/j.scitotenv.2022.155337

Shu, H., Hürlimann, M., Molowny-Horas, R., González, M., Pinyol, J., Abancó, C., & Ma, J. (2019). Relation between land cover and landslide susceptibility in Val d'Aran, Pyrenees (Spain): Historical aspects, present situation and forward prediction. *Science of The Total Environment, 693*, 133557. https://doi.org/10.1016/j.scitotenv.2019.07.363

Shu, H., Guo, Z., Qi, S., Song, D., Pourghasem, H. R., & Ma, J. (2021). Integrating landslide typology with weighted frequency ratio model for landslide susceptibility mapping: A case study from Lanzhou City of northwestern China. *Remote Sensing, 13*(18), 3623. https://doi.org/10.3390/rs13183623

Shugar, D. H., Jacquemart, M., Shean, D., et al. (2021). A massive rock and ice avalanche caused the 2021 disaster at Chamoli, Indian Himalaya. *Science, 373*(6552), 300–306. https://doi.org/10.1126/science.abh4455

Tang, H., Wasowski, J., & Juang, C. H. (2019). Geohazards in the three gorges reservoir area, China – lessons learned from decades of research. *Engineering Geology, 261*, 105267. https://doi.org/10.1016/j.enggeo.2019.105267

Taylor, F. E., Malamud, B. D., Freeborough, K., & Demeritt, D. (2015). Enriching Great Britain's National Landslide Database by searching newspaper archives. *Geomorphology, 249*, 52–68. https://doi.org/10.1016/j.geomorph.2015.05.019

Victoriano, A., García-Silvestre, M., Furdada, G., & Bordonau, J. (2016). Long-term entrenchment and consequences for present flood hazard in the Garona River (Val d'Aran, Central Pyrenees, Spain). *Natural Hazards and Earth System Sciecnes, 16*, 2055–2070. https://doi.org/10.5194/nhess-16-2055-2016

Xiao, Y., Ma, G., Wu, H., Lu, H., & Zaman, M. (2022). Rainfall-Induced Erosion of Biocemented Graded Slopes. *International Journal of Geomechanics, 22*(1), 04021256. https://doi.org/10.1061/(asce)gm.1943-5622.0002239

Xu, Y., Liao, X., Tang, L., & Li, L. (2024). Field Study of HPTRM Combined with Vegetation and Anchor to Protect Newly Excavated Expansive Soil Slope. *Journal of Earth Science, 35*(4), 1277–1288. https://doi.org/10.1007/s12583-021-1570-4

Yang, Z., Cheng, D., & Xia, J. (2024). Effects of the rainfall-triggered lisse effect on the stability of loess slopes. *Journal of Earth Science, 35*(4), 1254–1262. https://doi.org/10.1007/s12583-021-1536-6

Yin, Y. (2011). Recent catastrophic landslides and mitigation in China. *Journal of Rock Mechanics and Geotechnical Engineering, 3*(1), 10–18. https://doi.org/10.3724/SP.J.1235.2011.00010

Zhang, M., & McSaveney, M. J. (2018). Is air pollution causing landslides in China? *Earth and Planetary Science Letters, 481*, 284–289. https://doi.org/10.1016/j.epsl.2017.10.045

Zhang, S., Li, C., Peng, J., Zhou, Y., Wang, S., Chen, Y., & Tang, Y. (2023). Fatal landslides in China from 1940 to 2020: occurrences and vulnerabilities. *Landslides, 20*, 1243–1264. https://doi.org/10.1007/s10346-023-02034-6

Zhao, B., Su, L., Xu, Q., Li, W., Xu, C., & Wang, Y. (2023). A review of recent earthquake-induced landslides on the Tibetan Plateau. *Earth-Science Reviews, 244*, 104534. https://doi.org/10.1016/j.earscirev.2023.104534

Zhuang, J., Peng, J., Wang, G., Javed, I., Wang, Y., & Li, W. (2018). Distribution and characteristics of landslide in Loess Plateau: A case study in Shaanxi province. *Engineering Geology, 236*, 89–96. https://doi.org/10.1016/j.enggeo.2017.03.001

Zeng, T., Wu, L., Hayakawa, Y. S., Yin, K., Gui, L., Jin, B., ... Peduto, D. (2024). Advanced integration of ensemble learning and MT-InSAR for enhanced slow-moving landslide susceptibility zoning. *Engineering Geology, 331*, Article 107436. https://doi.org/10.1016/j.enggeo.2024.107436

Zêzere, J. L. (2002). Landslide susceptibility assessment considering landslide typology: A case study in the area north of Lisbon (Portugal). *Natural Hazards and Earth System Science, 2*, 73–82. https://doi.org/10.5194/nhess-2-73-2002